Nanostructures

International Edition: DOI: 10.1002/anie.201805890
German Edition: DOI: 10.1002/ange.201805890

# Creating Zipper-Like van der Waals Gap Discontinuity in Low-Temperature-Processed Nanostructured $PbBi_{2n}Te_{1+3n}$: Enhanced Phonon Scattering and Improved Thermoelectric Performance

*Biao Xu[+],* Tianli Feng[+], Zhe Li, Lin Zhou, Sokrates T. Pantelides, and Yue Wu**

***Abstract:*** *Nanoengineered materials can embody distinct atomic structures which deviate from that of the bulk-grain counterpart and induce significantly modified electronic structures and physical/chemical properties. The phonon structure and thermal properties, which can also be potentially modulated by the modified atomic structure in nanostructured materials, however, are seldom investigated. Employed here is a mild approach to fabricate nanostructured $PbBi_{2n}Te_{1+3n}$ using a solution-synthesized PbTe-$Bi_2Te_3$ nano-heterostructure as a precursor. The as-obtained monoliths have unprecedented atomic structure, differing from that of the bulk counterpart, especially the zipper-like van der Waals gap discontinuity and the random arrangement of septuple-quintuple layers. These structural motifs break the lattice periodicity and coherence of phonon transport, leading to ultralow thermal conductivity and excellent thermoelectric z T.*

The atomic structure of nanostructured materials can deviate significantly from that of the bulk phase having the same composition. For example, abnormal face-centered cubic (fcc) Ru,[1] body-centered cubic (bcc) α-AgI,[2] and hexagonal 4H Au,[3] rather than their regular hexagonal close-packed (hcp), hexagonal β, and fcc bulk counterparts, respectively, can be stabilized in the nanophase at room temperature, possibly because of the surface dangling bonds and defects. Further downsizing to 1–2 nm or sub-nanometer scales endows the nanocluster with a novel atomic arrangement that has never been observed in the bulk counterpart, as exemplified by bcc $Au_{38}$ clusters,[4] triangular $Ru_3$,[5] and so on. The resulting unique atomic structure can induce an unprecedented electronic structure and physical/chemical characteristics. For example, the nano α-AgI stabilized at room temperature showed superior ionic conductivity compared to the conventional bulk β phase.[2] $Au_{25}$ nanoclusters can reduce $Cu^{2+}$ to $Cu^0$, which cannot be done by bulk Au.[6]

Regarding the phonon structure and thermal transport properties that are also dictated by the atomic structure, the pertinent studies in the nanophase have been limited. Investigations of the nanosize effect on thermal transport has so far been limited to enhanced scattering of phonons at the nanoscale grain boundaries of either the matrix compound[7] or the nano-inclusion-matrix interfaces.[8] The influence of unusual atomic structure, induced by nanostructuring, on the thermal transport can shed light on various fields such as thermoelectrics and thermal insulation, but has been little studied.

$Bi_2Te_3$ is a predominant thermoelectric material near room temperature (300–500 K).[9] Its small band gap (ca. 0.16 eV) causes unwanted bipolar thermal conduction, a diminished Seebeck coefficient, and deteriorated $zT$ at higher temperatures. A wealth of studies[10] attempted to combine $Bi_2Te_3$ with metal tellurides having a larger $E_g$ (SnTe, PbTe) to yield ternary compounds ($SnBi_2Te_4$, $PbBi_4Te_7$, and $PbBi_6Te_{10}$, and so on) with better performance in the mid-temperature range (500–700 K). The complex many-atom-layered structure and alloying effect further diminished the lattice thermal conductivity ($0.70\ Wm^{-1}K^{-1}$ in the case of $PbBi_4Te_7$ at 300 K[10a]) as compared to binary $Bi_2Te_3$ ($1.4\ Wm^{-1}K^{-1}$ at 300 K[11]). However, a solid-state high-temperature reaction was adopted for these syntheses, and the microstructures on the atomic, nano, and microscales were not well manipulated. Therefore, these bulk-phase materials exhibit unsatisfactory $zT < 1.0$, leaving plenty of room for optimization.

In this study, we employ solution-synthesized PbTe-$Bi_2Te_3$ nano-heterostructures as a starting powder and conduct subsequent low-temperature sintering to obtain nanostructured monoliths of $PbBi_{2n}Te_{1+3n}$. The ambient reaction conditions lead to an extraordinary atomic structure differing from the bulk counterpart, and it is revealed through electron microscopy. Density-functional theory (DFT) calculations explain the formation mechanism of the novel atomic structure. Calculations based on molecular dynamics (MD) and the Boltzmann transport equation (BTE) elucidate how the structural motifs reduce the lattice thermal conductivity and improve the thermoelectric figure of merit. This mild approach may be widely applicable to the synthesis of nanostructured complex compounds in which the atomic structure may deviate from that of the corresponding bulk

[*] Prof. Dr. B. Xu[+]
School of Chemical Engineering, Nanjing University of Science and Technology, Nanjing, Jiangsu 210094 (China)
E-mail: xubiao@njust.edu.cn
Z. Li, Prof. Dr. Y. Wu
Department of Chemical and Biological Engineering, Iowa State University, Ames, IA 50011 (USA)
E-mail: yuewu@iastate.edu
Dr. T. L. Feng,[+] Prof. Dr. S. T. Pantelides
Department of Physics and Astronomy and Department of Electrical Engineering and Computer Science, Vanderbilt University
Nashville, TN 37235 (USA)
Prof. Dr. L. Zhou
Ames Laboratory, Department of Energy
Ames, IA 50011 (USA)
[+] These authors contributed equally to this work.
Supporting information and the ORCID identification number(s) for the author(s) of this article can be found under: https://doi.org/10.1002/anie.201805890.

  

counterpart, and have modulated phonon and thermoelectric properties.

The synthesis of the $x$PbTe-(1−$x$) $Bi_{0.666}Te$ nano-heterostructure (NHS) was inspired by the previous method using a topotactic reaction.[12] The procedures are described in the Supporting Information. The products in each intermediate step were comprehensively characterized (see Figures S1a–e in the Supporting Information). In the X-ray diffraction (XRD) profile (Figure 1 a), rock-salt PbTe and rhombohedral $Bi_2Te_3$ were indexed in the as-synthesized PbTe-$Bi_{0.666}Te$ NHS. The morphology of a dumbbell structure (see Figure S1d) and crystallographic orientation (see Figure S1f and g) were observed in transmission electron microscopy (TEM). The scalable production (11 grams per batch) of the PbTe-$Bi_2Te_3$ NHS allowed the consolidation of the powder into a macroscopic ingot for thermoelectric application. After spark plasma sintering (SPS), the as-obtained monolith was characterized to study its composition and microstructure. First, an energy dispersive spectrum (EDS), collected from an area of 25 μm × 20 μm (see Figure S2), on the nano $PbBi_4Te_7$ sample indicated that Pb, Bi, and Te are uniformly distributed throughout the sample. EDS detected the atomic ratio of Pb/Bi/Te = 8.31:33.89:57.80, which corresponds to $PbBi_{4.08}Te_{6.96}$ and agrees well with the nominal $PbBi_4Te_7$. In the XRD profile (Figure 1 a; see magnified view in Figure S3), the peaks of rock-salt PbTe disappeared after SPS, indicating its complete reaction with $Bi_2Te_3$. The product was indexed as $PbBi_4Te_7$ (JCPDS: 44-1439).

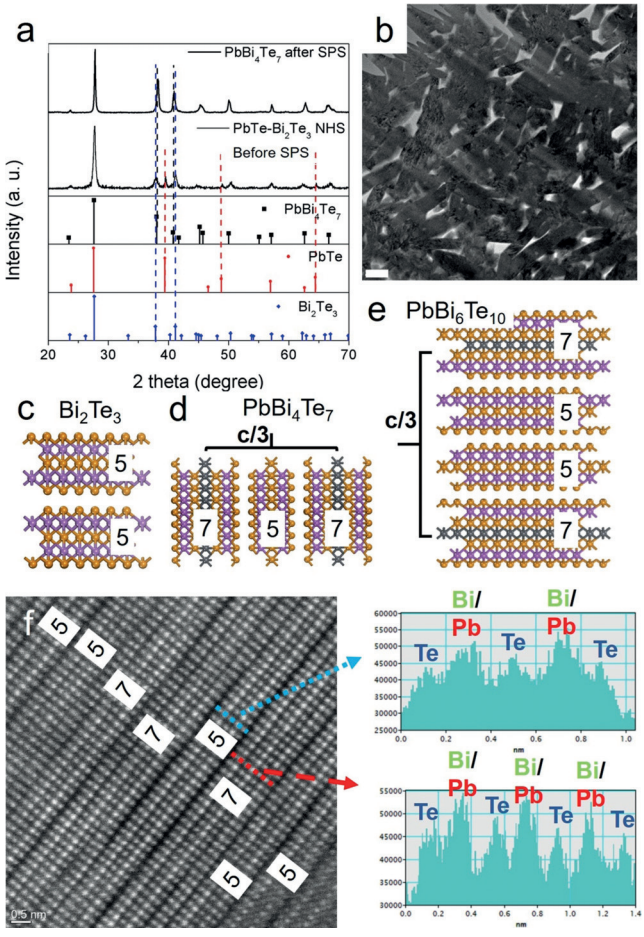


***Figure 1.*** a) XRD profiles of the 0.14286 PbTe-0.85714 $Bi_{0.666}Te$ NHS before SPS and nano $PbBi_4Te_7$ sample after SPS. b) HRTEM image of the nano $PbBi_6Te_{10}$ sample. Scale bar is 100 nm. Illustrations of bulk-phase crystal structures of c) $Bi_2Te_3$, d) $PbBi_4Te_7$, and e) $PbBi_6Te_{10}$. The Pb, Bi, and Te atoms are represented by the grey, purple, and orange balls, respectively. f) HAADF-STEM image of nano $PbBi_6Te_{10}$ with line-intensity profiles showing the quintuple and septuple atomic layers, scale bar is 0.5 nm.

$Bi_2Te_3$ is composed of quintuple Te-Bi-Te-Bi-Te layers stacking along the c-axis and separated by van der Waals (vdW) gaps (Figure 1 c, 5-5-5…). If equal-stoichiometry PbTe and $Bi_2Te_3$ are combined as $PbBi_2Te_4$, it comprises Te-Bi-Te-Pb-Te-Bi-Te septuple layers (7-7-7…), in which a Pb-Te layer is inserted into the middle of each $Bi_2Te_3$ quintuple layer. If PbTe and double-stoichiometry $Bi_2Te_3$ are mixed, the resulting $PbBi_4Te_7$ (Figure 1 d)[10a] is made of periodic 5-7-5-7-5-7… layers ($Bi_2Te_3$-$PbBi_2Te_4$…). Similarly, PbTe and triple-stoichiometry $Bi_2Te_3$ yield the $PbBi_6Te_{10}$, which exhibits a 5-5-7-5-5-7… structure[13] ($Bi_2Te_3$-$Bi_2Te_3$-$PbBi_2Te_4$…; Figure 1 e). The standard XRD pattern of $PbBi_4Te_7$ (Figure 1 a, solid black lines; also see Figure S3) is similar to that of $Bi_2Te_3$ (Figure 1 a, solid blue lines; also see Figure S3) and showed slight deviations, because the layered structures of homologous $PbBi_{2n}Te_{1+3n}$ ($n$ = 1, 2, 3) are derived from $Bi_2Te_3$. Moreover, we have found that the XRD peaks of the nano $PbBi_4Te_7$ sample shift a little bit with respect to the standard lines of the bulk phase (see Figure S3) because of the deviation of the nanophase atomic structure as compared to bulk-phase counterpart, as will be carefully discussed later. Similar EDS (detected: $PbBi_{6.14}Te_{9.92}$) and XRD results (see Figure S4) could be found in the nano $PbBi_6Te_{10}$ sample as well. HRTEM of the focused-ion-beam-milled thin section reveals abundant pores and nanosized grains (Figure 1 b). A layered grain structure of $PbBi_{2n}Te_{1+3n}$ could be observed in the HRTEM (see Figure S7). The average grain size of the nano $PbBi_6Te_{10}$ sample was estimated as 70 nm along the c axis and 140 nm along $a$/$b$ axis. Porosity was calculated as 16 % based on the relative density (84 %).

As a control experiment, we performed SPS of a mixture of bulk PbTe (325 mesh, size ca. 44 μm) and $Bi_2Te_3$ (325 mesh). Under the same sintering conditions, the XRD of the bulk-phase product explicitly showed the peaks of PbTe and $Bi_2Te_3$ (see Figure S8), without any discernible peaks of $PbBi_4Te_7$, indicating that almost no solid-state reaction happened. Although there has been almost no study on the diffusion of Bi into PbTe, a previous study on diffusion of Na into PbTe[14] revealed that it takes around 280 s (4.67 min) for a migration length of 70 nm at 650 K. This result implies that only the surface (depth around 70 nm) layer of bulk-grain (44 μm) PbTe and $Bi_2Te_3$ may diffuse into and react with each other during 5 minutes of SPS at 698 K, thus explaining the absence of peaks of $PbBi_4Te_7$. Previous studies used high-temperature, long-time, solid-state reactions[10a,13] (1070 K for 5 h, then 770 K for 1000 h) to obtain bulk-grain phase-pure $PbBi_4Te_7$ and $PbBi_6Te_{10}$. The present result that nano $PbBi_4Te_7$ and $PbBi_6Te_{10}$ could be synthesized at only 698 K within 5 minutes underscores the advantage of a solution-synthesized NHS as an efficient precursor to yield ternary compounds.

  

Aside from the time efficiency, the mild nanoscale reaction also facilitates stabilization of extraordinary atomic structure because of dissimilar reaction kinetics and thermodynamics as compared with the bulk counterpart. As implied from the single-crystal structure of bulk-phase $PbBi_6Te_{10}$,[13] the final product should exhibit a periodic 5-5-7-5-5-7… structure, in which Pb is located in the middle of the septuple layer and vdW gaps are inserted between these two-dimensional (2D) layers (Figure 1e). Contrarily, several intriguing structures in the nanoproduct of $PbBi_6Te_{10}$ (or $PbBi_4Te_7$), structures which deviate from that of the bulk counterpart (Figure 1d and e), were observed in HAADF-STEM. First, the quintuple and septuple layer are not periodically arranged. Instead, some random arrangement of the layers [for example, 5-5-7-7-5-7-5-5 in Figure 1f (nano $PbBi_6Te_{10}$) and 7-7-5-7-7-7 (nano $PbBi_4Te_7$) in Figure S9] could be found. Second, the septuple layers were deformed frequently, forming a zipper-like vdW gap discontinuity. As shown in Figures 2a and b, the vdW gaps between quintuple and septuple layers were sometimes nonconsecutive as highlighted in the dashed yellow boxes. Third, as indicated from the atomic-level EDS mapping in Figure 2c (see Figures S10a and S10b), on at least a 10 nanometer scale, Pb and Bi are randomly occupying the octahedral sites between the Te atom columns rather than staying in particular atomic rows as in the single-crystal structure of $PbBi_4Te_7$ (Figure 1d) and $PbBi_6Te_{10}$ (Figure 1e). Although this Pb-Bi random occupancy was proposed as possible in previous XRD refinement studies[13] of bulk $PbBi_4Te_7$, herein we provide the visual evidence using local-probe investigation. Fourth, the vdW gap frequently vanished (see Figure 2b, green dashed rectangle) after incorporation of PbTe into $Bi_2Te_3$. $Bi_2Te_3$ can be viewed as the remaining lamella after exfoliating 1/3 of the Bi layers from imaginary "rock-salt BiTe" (Figure S10c). Therefore, the alloying of PbTe with $Bi_2Te_3$ seemed to heal the vdW gap of $Bi_2Te_3$ to revert to the non-gapped rock-salt structure.

To understand the physical origins of these extraordinary structures, we have conducted comprehensive DFT calculations. 1) The tentative mechanism of the formation of the zipper-like nonconsecutive vdW gaps between quintuple and septuple layers is shown in Figure 2d–f. Figure 2d shows the nondistorted vdW gaps between quintuple and septuple layers. Figure 2e shows that half of the Bi-Te layer near the gap is flipped up to form a zipper-like structure. This proposed structure agrees well with the HADDF-STEM Z-contrast of Bi/Pb (brighter atoms, purple circled) and Te (darker atoms, yellow circled), whose sites gradually exchange with each other at the boundary of zipper-like structures (Figure 2b: see magnified view in Figure S11). Figure 2f shows a configuration that the whole Bi-Te layer near the vdW gap is flipped up. All the three structures in Figures 2d–f are governed by the quintuple-septuple (5-7) layer interaction as marked by the green double-headed arrows. Therefore, they have similar formation energy. DFT calculations reveal that the configuration in Figure 2e is only 0.031 eV/pair-Bi-Te atoms higher than those in Figures 2d and f. This result indicates that the structures in Figure 2d–f can all be formed during synthesis and explains why the zipper-like structure can be commonly seen in $PbBi_{2n}Te_{1+3n}$ samples. In contrast, it cannot exist if Pb is not introduced into the system, that is, if there are no septuple layers. As shown in Figures 2g–i, $Bi_2Te_3$ is composed of quintuple layers only, between which the flipping of Bi-Te layer near the vdW gap leads to an interaction between 7-3. Our DFT calculations reveal that the 7-3 formation energy is 0.593 eV/pair-Bi-Te atoms higher than that of the original 5-5 configurations and much larger than the thermal fluctuation (698 K, $k_B T = 0.060$ eV). Therefore, the zipper-like nonconsecutive vdW gaps possibly exist only in $PbBi_{2n}Te_{1+3n}$ rather than in $Bi_2Te_3$. 2) The 5-7 layer randomness can be explained by the mechanism of the formation of zipper-like structure: the switch of the order from 5-7 to 7-5 (Figure 2d and f) can be realized through an intermediate state of the zipper-like gap (Figure 2e) and is energetically favorable. Besides, we have directly calculated the energy difference between the ordered- and random-thickness structures (see Figure S12) to be trivial (0.0015 eV/atom).

The thermoelectric properties of several samples having different Pb contents were measured along the SPS pressing direction (cross-plane). No significant anisotropy was found either along the cross-plane or the in-plane direction (see Figure S14). The absolute values of the Seebeck coefficient ($S$) of the nano $PbBi_{12.666}Te_{20}$, $PbBi_6Te_{10}$, and $PbBi_4Te_7$ samples all steadily increased with ascending temperatures before

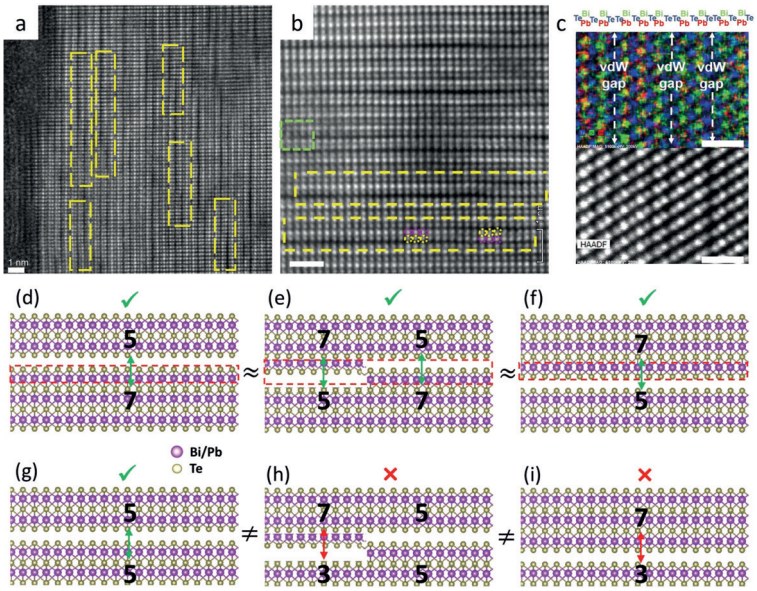


***Figure 2.*** a,b) The HAADF-STEM images of nano $PbBi_6Te_{10}$ and $PbBi_4Te_7$ samples, respectively. Zipper-like structures are highlighted by the yellow dashed boxes. Purple and yellow dashed circles in (b) represent Bi/Pb (brighter) and Te (darker) atoms, respectively. The green dash box in (b) highlights vanishing of van der Waals gap. c) Atomic-level element mapping of nano $PbBi_4Te_7$. The red, green, and blue dots correspond to Pb, Bi, and Te atoms, respectively. d–f) The mechanism of the formation of zipper-like structures between quintuple and septuple layers in $PbBi_4Te_7$. g–i) Schematic illustrations that the zipper-like structure cannot be formed between two quintuple layers in $Bi_2Te_3$. All the scale bars are 1 nm in (a–c).

  

saturation at 600–700 K (Figure 3a, hollow symbols). This result indicates that they behave like heavily doped degenerate semiconductors and the minority-carrier contribution to the Seebeck coefficient starts to play a role in the high-temperature range.[12] The electrical conductivity ($\sigma$) decreased with increasing temperature and the slopes of $\sigma$–$T$ varied in different samples, implying slightly different mechanisms of charge carrier scattering (Figure 3a, solid symbols).[15] The $\sigma$ of the $PbBi_{12.666}Te_{20}$ sample (Figure 3a, blue solid triangles) started to ascend with respect to increasing $T$ at greater than 500 K, possibly because of the bipolar electronic conduction. This result agrees well with the saturation of $S$ of the $PbBi_{12.666}Te_{20}$ sample at greater than 500 K (Figure 3a, blue hollow triangles). The power factors were calculated as $S^2\sigma$ and displayed in Figure 3b. The highest power factor attained was 0.99 $mWm^{-1}K^{-2}$ at 688 K for the nano $PbBi_4Te_7$ sample.

The total thermal conductivity ($\kappa_{total}$; Figure 3c) was calculated as $D_t \times \rho \times C_p$, in which $D_t$ (thermal diffusivity) was measured using a laser flash method, $\rho$ (mass density) was determined geometrically, and $C_p$ (specific heat) was measured using differential scanning calorimetry (DSC). The electronic contribution to thermal conductivity ($\kappa_e$) is estimated using the Wiedemann Franz Law, $\kappa_e = L\sigma T$, in which $L$ (Lorenz number) is calculated according to an empirical formula ($L = 1.5 + \exp(-|S|/116)$, $L$ is in $10^{-8}\,W\Omega K^{-2}$).[16] As shown in Figure 4a, the lattice thermal conductivities ($\kappa_{total}-\kappa_e$) of nano $PbBi_{2n}Te_{1+3n}$ ($n = 6.333$, 3 and 2) samples are around 0.18–0.21 $Wm^{-1}K^{-1}$ at 313 K, and are much lower than those of the bulk-grain counterpart[10a] (0.70 $Wm^{-1}K^{-1}$ for $PbBi_4Te_7$ and 0.85 $Wm^{-1}K^{-1}$ for $PbBi_6Te_{10}$). Such huge drops of lattice thermal conductivity might originate from the intriguing microstructures: 1) the Pb-Bi site randomness, 2) nanograins, 3) nanopores, and 4) the nonconsecutive vdW gaps as well as the random arrangement of quintuple or septuple multilayers.

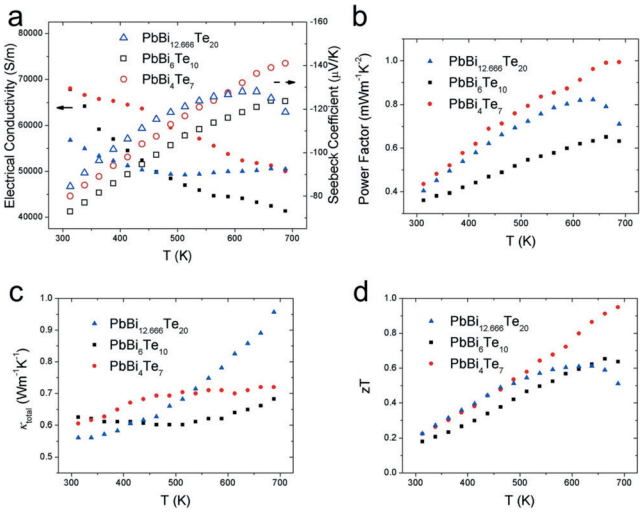


***Figure 3.*** Temperature-dependent a) electrical conductivity (left axis, solid symbols), Seebeck coefficient (right axis, hollow symbols), b) power factor, and c) total thermal conductivity. d) Figure of merit of the nano $PbBi_{12.666}Te_{20}$ (triangles), $PbBi_6Te_{10}$ (squares), and $PbBi_4Te_7$ (circles) samples.

To quantitatively estimate the impacts of these microstructures on lattice thermal conductivity ($\kappa_l$), we have conducted phonon Boltzmann transport equation (BTE) modeling and molecular dynamics (MD) simulations to study the first three and the last impacts, respectively (details are shown in the Supporting Information). The thermal conductivity reductions resulting from the Pb-Bi site randomness, nanograin boundaries (GB), and pores for $PbBi_4Te_7$ are shown in Figure 4c for $PbBi_4Te_7$. Similar results for $PbBi_6Te_{10}$ are shown in Figure S16. The mass disorder induced by Pb-Bi location randomness has trivial impact on thermal conductivity since the mass difference between Pb and Bi elements is small. In contrast, the nanograin boundaries and pores[17] induce significant reduction on $\kappa_l$ as a result of the small grain size (averaged 229 nm for $PbBi_4Te_7$ and 138 nm for $PbBi_6Te_{10}$) and high porosity (ca. 16%). The nanograin boundaries and pores of the $PbBi_4Te_7$ sample reduce $\kappa_l$ from 0.70 $Wm^{-1}K^{-1}$ to 0.30 $Wm^{-1}K^{-1}$, which is still much higher than the experimental $\kappa_{tot}-\kappa_e$ (0.18 $Wm^{-1}K^{-1}$). The difference may result from the random arrangement of quintuple-septuple layers and the nonconsecutive vdW gaps that break the coherence of phonon transport.

As this effect cannot be modelled by phonon BTE, we conducted MD simulations. As shown in Figure 4b, in periodic superlattices, the heat conduction is composed of coherent and incoherent components, with the former one depending on the wave nature of phonons and the periodicity

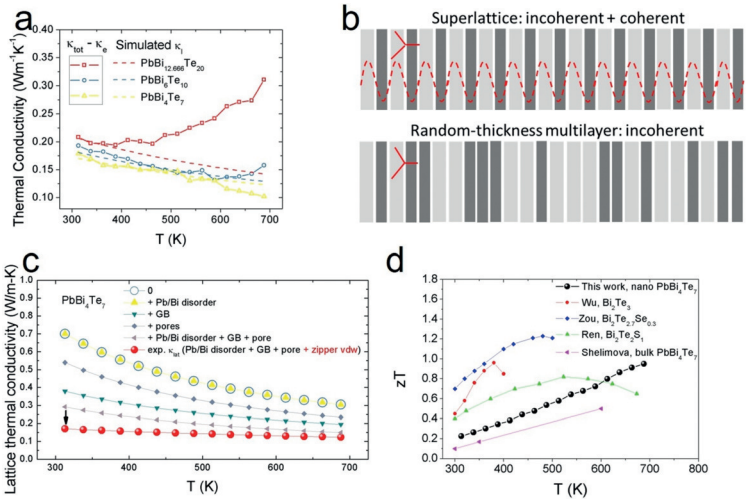


***Figure 4.*** a) $\kappa_{tot}-\kappa_e$ of $PbBi_{12.666}Te_{20}$ (hollow squares), $PbBi_6Te_{10}$ (hollow circles), and $PbBi_4Te_7$ (hollow triangles) and simulated $\kappa_l$ (dash lines). b) Schematic illustration that the 5-7 random multilayers can break the coherent phonon transport in superlattice. The light and dark grey columns represent septuple and quintuple layers, respectively of $PbBi_4Te_7$. c) BTE simulation of $\kappa_l$ of the nano $PbBi_4Te_7$ sample considering several structural factors. d) $zT$ of present nano $PbBi_4Te_7$ (black spheres) as compared to that of $Bi_2Te_3$,[21] $Bi_2Te_{2.7}Se_{0.3}$,[22] $Bi_2Te_2S_1$,[11] and bulk $PbBi_4Te_7$[10a] samples.

  

of the lattice.[18] It has been found that the loss of periodicity in terms of layer thickness can eliminate the coherent heat conduction contribution and largely reduce the lattice thermal conductivity in hypothetical Lennard-Jones superlattice[19] and Si/Ge superlattices.[20] Here, since there are no available interatomic potentials for $PbBi_{2n}Te_{1+3n}$, we use those for $Bi_2Te_3$ instead, and change the mass of partial Bi to model the septuple layers (the details of modeling can be found in the Supporting Information). This rough model reveals that the break of coherence from the periodic structure to the nonperiodic one can reduce the thermal conductivity by 25%.

Aside from the lattice and electronic thermal conductivities, the bipolar thermal conductivity is also important in $Bi_2Te_3$-derived compounds.[12,17] From Figure 4a, the upward turn of $\kappa_{tot}-\kappa_e$ with increasing temperature at 500–700 K is due to the bipolar contribution, and is suppressed as the content of PbTe increases and the $E_g$ of $PbBi_{2n}Te_{1+3n}$ is enlarged, because PbTe has a larger $E_g$ (0.31 eV) than $Bi_2Te_3$ (0.16 eV).

Collectively, the thermoelectric figure of merit, $zT$, is calculated as $S^2\sigma T/\kappa$ (Figure 3d). The highest $zT$ attained is 0.95 at 688 K in the nano $PbBi_4Te_7$ sample. When compared to conventional n-type $Bi_2Te_3$ (Figure 4d, red line)[21] and other types of n-type alloyed $Bi_2Te_3$, such as $Bi_2Te_{2.7}Se_{0.3}$ (blue line in Figure 4d),[22] $Bi_2Te_2S_1$ (green line in Figure 4d),[11] the peak temperature of $zT$ of the nano $PbBi_4Te_7$ sample is shifted to higher values (600–700 K) because of the enlarged band gap and suppressed bipolar conduction. As compared to bulk-grain $PbBi_4Te_7$ material, the aforementioned hierarchical structural factors can substantially reduce $\kappa_l$ of the nano $PbBi_4Te_7$ sample. This reduction in $\kappa_l$ leads to enhanced $zT$ of the nano $PbBi_4Te_7$ sample as compared to the bulk counterpart (magenta line in Figure 4d), qualifying it as a promising n-type candidate to convert the medium-temperature waste heat into electricity.

In summary, we employed a bottom-up wet chemical approach to synthesize nano $PbBi_{2n}Te_{1+3n}$ ($n = 6.333$, 3 and 2) samples under ambient conditions. The extraordinary atomic structure deviating from that of bulk-grain counterpart is revealed by HAADF-STEM and explained by DFT simulations. At multiple length scales, the unique atomic structure, nanograins, and nanopores together lead to extremely low lattice thermal conductivity of the nano $PbBi_4Te_7$ sample. As a result, its high $zT$ in the range of 600–700 K qualifies this material as a promising candidate for medium-temperature thermoelectrics. This study is likely to have broad impact on other intriguing 2D van der Waals nanostructures for applications in thermoelectrics, catalysis, optoelectronics, and so on.

## Acknowledgements

B.X. acknowledges support from startup funding of Nanjing University of Science and Technology (AE89991/043). Z. Li. and Y.W. thank the support from ACRI Center Initiative from Iowa State University and Herbert L. Stiles Professorship. Work at Vanderbilt (T.L.F., S.T.P.) was supported in part by Department of Energy grant DE-FG0209ER46554 and by the McMinn Endowment. Computations at Vanderbilt University and ORNL were performed at the National Energy Research Scientific Computing Center (NERSC), a Department of Energy, Office of Science, User Facility funded through Contract No. DE-AC02-05CH11231. Computations also used the Extreme Science and Engineering Discovery Environment (XSEDE).

## Conflict of interest

The authors declare no conflict of interest.

**Keywords:** atomic structure · materials science · nanostructures · phonons · tellurium

**How to cite:** *Angew. Chem. Int. Ed.* **2018**, *57*, 10938–10943
*Angew. Chem.* **2018**, *130*, 11104–11109

[1] a) M. Zhao, A. O. Elnabawy, M. Vara, L. Xu, Z. D. Hood, X. Yang, K. D. Gilroy, L. Figueroa-Cosme, M. Chi, M. Mavrikakis, Y. Xia, *Chem. Mater.* **2017**, *29*, 9227–9237; b) K. Kusada, H. Kobayashi, T. Yamamoto, S. Matsumura, N. Sumi, K. Sato, K. Nagaoka, Y. Kubota, H. Kitagawa, *J. Am. Chem. Soc.* **2013**, *135*, 5493–5496.

[2] R. Makiura, T. Yonemura, T. Yamada, M. Yamauchi, R. Ikeda, H. Kitagawa, K. Kato, M. Takata, *Nat. Mater.* **2009**, *8*, 476.

[3] Z. Fan, M. Bosman, X. Huang, D. Huang, Y. Yu, K. P. Ong, Y. A. Akimov, L. Wu, B. Li, J. Wu, Y. Huang, Q. Liu, C. Eng Png, C. Lip Gan, P. Yang, H. Zhang, *Nat. Commun.* **2015**, *6*, 7684.

[4] C. Liu, T. Li, G. Li, K. Nobusada, C. Zeng, G. Pang, L. Rosi Nathaniel, R. Jin, *Angew. Chem. Int. Ed.* **2015**, *54*, 9826–9829; *Angew. Chem.* **2015**, *127*, 9964–9967.

[5] S. Ji, Y. Chen, Q. Fu, Y. Chen, J. Dong, W. Chen, Z. Li, Y. Wang, L. Gu, W. He, C. Chen, Q. Peng, Y. Huang, X. Duan, D. Wang, C. Draxl, Y. Li, *J. Am. Chem. Soc.* **2017**, *139*, 9795–9798.

[6] Z. Wu, *Angew. Chem. Int. Ed.* **2012**, *51*, 2934–2938; *Angew. Chem.* **2012**, *124*, 2988–2992.

[7] B. Poudel, Q. Hao, Y. Ma, Y. Lan, A. Minnich, B. Yu, X. Yan, D. Wang, A. Muto, D. Vashaee, X. Chen, J. Liu, M. S. Dresselhaus, G. Chen, Z. Ren, *Science* **2008**, *320*, 634–638.

[8] a) K. F. Hsu, S. Loo, F. Guo, W. Chen, J. S. Dyck, C. Uher, T. Hogan, E. K. Polychroniadis, M. G. Kanatzidis, *Science* **2004**, *303*, 818–821; b) W. Kim, J. Zide, A. Gossard, D. Klenov, S. Stemmer, A. Shakouri, A. Majumdar, *Phys. Rev. Lett.* **2006**, *96*, 045901.

[9] a) H. J. Goldsmid, R. W. Douglas, *Br. J. Appl. Phys.* **1954**, *5*, 386; b) C. B. Satterthwaite, R. W. Ure, *Phys. Rev.* **1957**, *108*, 1164–1170.

[10] a) L. E. Shelimova, O. G. Karpinskii, P. P. Konstantinov, E. S. Avilov, M. A. Kretova, V. S. Zemskov, *Inorg. Mater.* **2004**, *40*, 451–460; b) L. Pan, J. Li, D. Berardan, N. Dragoe, *J. Solid State Chem.* **2015**, *225*, 168–173; c) T. Schäfer, P. M. Konze, J. D. Huyeng, V. L. Deringer, T. Lesieur, P. Müller, M. Morgenstern, R. Dronskowski, M. Wuttig, *Chem. Mater.* **2017**, *29*, 6749–6757.

[11] W. Liu, K. C. Lukas, K. McEnaney, S. Lee, Q. Zhang, C. P. Opeil, G. Chen, Z. Ren, *Energy Environ. Sci.* **2013**, *6*, 552–560.

[12] B. Xu, M. T. Agne, T. Feng, T. C. Chasapis, X. Ruan, Y. Zhou, H. Zheng, J. H. Bahk, M. G. Kanatzidis, G. J. Snyder, *Adv. Mater.* **2017**, *29*, 1605140.

[13] O. G. Karpinskii, L. E. Shelimova, E. S. Avilov, M. A. Kretova, V. S. Zemskov, *Inorg. Mater.* **2002**, *38*, 17–24.

[14] K. Biswas, J. He, I. D. Blum, C.-I. Wu, T. P. Hogan, D. N. Seidman, V. P. Dravid, M. G. Kanatzidis, *Nature* **2012**, *489*, 414–418.

  

[15] L. Pan, S. Mitra, L. D. Zhao, Y. Shen, Y. Wang, C. Felser, D. Berardan, *Adv. Funct. Mater.* **2016**, *26*, 5149 – 5157.
[16] H.-S. Kim, Z. M. Gibbs, Y. Tang, H. Wang, G. J. Snyder, *APL Mater.* **2015**, *3*, 041506.
[17] B. Xu, T. Feng, M. T. Agne, L. Zhou, X. Ruan, G. J. Snyder, Y. Wu, *Angew. Chem. Int. Ed.* **2017**, *56*, 3546 – 3551; *Angew. Chem.* **2017**, *129*, 3600 – 3605.
[18] M. N. Luckyanova, J. Garg, K. Esfarjani, A. Jandl, M. T. Bulsara, A. J. Schmidt, A. J. Minnich, S. Chen, M. S. Dresselhaus, Z. Ren, E. A. Fitzgerald, G. Chen, *Science* **2012**, *338*, 936.
[19] Y. Wang, C. Gu, X. Ruan, *Appl. Phys. Lett.* **2015**, *106*, 073104.
[20] B. Qiu, G. Chen, Z. Tian, *Nanoscale Microscale Thermophys. Eng.* **2015**, *19*, 272.
[21] G. Zhang, B. Kirk, L. A. Jauregui, H. Yang, X. Xu, Y. P. Chen, Y. Wu, *Nano Lett.* **2012**, *12*, 56 – 60.
[22] M. Hong, T. C. Chasapis, Z.-G. Chen, L. Yang, M. G. Kanatzidis, G. J. Snyder, J. Zou, *ACS Nano* **2016**, *10*, 4719 – 4727.

Manuscript received: May 21, 2018
Accepted manuscript online: June 27, 2018
Version of record online: July 20, 2018

  

Angewandte Chemie
Eine Zeitschrift der Gesellschaft Deutscher Chemiker

Supporting Information

# Creating Zipper-Like van der Waals Gap Discontinuity in Low-Temperature-Processed Nanostructured $PbBi_{2n}Te_{1+3n}$: Enhanced Phonon Scattering and Improved Thermoelectric Performance

*Biao Xu[+],* Tianli Feng[+], Zhe Li, Lin Zhou, Sokrates T. Pantelides, and Yue Wu**

anie_201805890_sm_miscellaneous_information.pdf

## Experimental Procedures

### Reagents

Tellurium dioxide ($TeO_2$, 99.995%), potassium hydroxide (KOH, 99.99%), polyvinylpyrrolidone (PVP, $M_w$ = 40,000), lead acetate trihydrate ($Pb(CH_3COO)_2{\cdot}3H_2O$, 99.99%), bismuth nitrate pentahydrate ($Bi(NO_3)_3{\cdot}5H_2O$, 99.99%), hydrazine hydrate aqueous solution ($N_2H_4{\cdot}H_2O$, 78-82%), anhydrous hydrazine ($N_2H_4$, 98%) and ethylene glycol (EG, 99%) are purchased from Sigma-Aldrich. Deionized water and absolute ethanol are used for centrifugation.

### Synthesis

#### The 0.10 PbTe-0.90 $Bi_{0.666}Te$ nanoheterostructure

First, 45 mmol (7.1820 g) of $TeO_2$, 600 mmol (33.6600 g) of KOH and 9.00 g of PVP ($M_w$ = 40,000) are dissolved into 450 mL of ethylene glycol (EG). The solution is heated to 100°C and then 7.5 mL of hydrazine hydrate solution (80%) is injected using a syringe. It turns into dark blue slurry and is kept at 100°C for 1 hour before the temperature is raised to 110°C. Te nanowire is formed at this step.

In the second step, the stock solution of lead acetate trihydrate (4.5 mmol (1.7063 g) of $Pb(OAc)_2{\cdot}3H_2O$ in 25 mL of EG) is added dropwise into the hot dispersion of Te nanowire. Then another 1 hour of heating is maintained at 110°C for the formation of PbTe-Te-PbTe nanoheterostructure.

Finally, the ethylene glycol solution (80 mL) of Bi precursor (27 mmol (13.0969 g) of $Bi(NO_3)_3{\cdot}5H_2O$) is heated to 140°C on a hot plate and then added in drop by drop, with precedent injection of anhydrous hydrazine (13.0 mL of $N_2H_4$) assisting the reduction of Bi. The whole slurry is heated at 110°C for 1 hour and then incubated at 140°C for another 0.5 h for the production of 0.10 PbTe-0.90 $Bi_{0.666}Te$ nanoheterostructure.

#### The 0.05 PbTe-0.95 $Bi_{0.666}Te$ and 0.14286 PbTe-0.85714 $Bi_{0.666}Te$ nanoheterostructure.

All the parameters are the same as those in the synthesis of **the 0.10 PbTe-0.90 $Bi_{0.666}Te$ nanoheterostructure**, except for the amount of Pb and Bi precursors. For the **0.05 PbTe-0.95 $Bi_{0.666}Te$,** 2.25 mmol (0.8532 g) of $Pb(OAc)_2{\cdot}3H_2O$ and 28.5 mmol (13.8245 g) of $Bi(NO_3)_3{\cdot}5H_2O$ were used. For the **0.14286 PbTe-0.85714 $Bi_{0.666}Te$ nanoheterostructure,** 6.4286 mmol (2.7423 g) of $Pb(OAc)_2{\cdot}3H_2O$ and 25.7142 mmol (12.4732 g) of $Bi(NO_3)_3{\cdot}5H_2O$ were used.

#### The $Bi_2Te_3$ nanowire

All the parameters are the same as those in the synthesis of **the 0.10 PbTe-0.90 $Bi_{0.666}Te$ nanoheterostructure**, except for the amount of Pb and Bi precursors. None of $Pb(OAc)_2{\cdot}3H_2O$ was used and 30 mmol (14.5521 g) $Bi(NO_3)_3{\cdot}5H_2O$ was used.

### Removing surfactants

The product from solution synthesis is washed with water and centrifuged for 3 times. Then the precipitate is re-dispersed in a ethanol solution (600 mL) of hydrazine hydrate (8% (v/v)) and stirred for 24 hours to strip off the surface-bound PVP. After that, the dispersion is washed with ethanol for another 3 times. Then the paste is vacuum-pumped overnight to yield dry powder. The dried solid is about 11.0 grams.

### Spark Plasma Sintering

The as-dried powder is loaded into a *Φ*-10.0 mm graphite die and then set up in a Fuji-211*lx* spark plasma sintering (SPS) system. SPS condition is as follows: axial pressure 40 MPa, sintering temperature 450°C and duration 5 min. After sintering, the graphite die should be cooled down at a slow rate (20°C/min).

For the $PbBi_{12.6666}Te_{20}$ pellet, the 0.05 PbTe-0.95 $Bi_{0.666}Te$ nano powder was used as precursor. For the $PbBi_6Te_{10}$ pellet, The 0.10 PbTe-0.90 $Bi_{0.666}Te$ nano powder was the precursor. For the $PbBi_4Te_7$ pellet, 0.14286 PbTe-0.85714 $Bi_{0.666}Te$ nanoheterostructure was used as the precursor.

**Characterizations**

X-ray diffraction (XRD) is recorded on a Rigaku Ultima U4, with Cu Kα radiation ($\lambda$ = 1.5418 Å), at 40 kV and 44 mA. Transmission Electron Microscopy (TEM) is acquired on a JEOL 2100F at 200 kV and a FEI Titan Themis 60-300 TEM ($C_s$-corrected) at 200 kV. Thin-section samples of the as-sintered pellet for TEM were fabricated using a focused ion beam (FIB, Helios Dual Beam, FEI). Scanning Electron Microscopy (SEM) is conducted on a FEI Quanta 250, with Energy Dispersion Spectra (EDS, Oxford Instrument).

**Thermoelectric Properties**

The samples are placed between a cold and a hot end while the temperature gradient and the electrical voltage across the two ends are simultaneously measured to calculate the Seebeck coefficients ($S$), in a Linseis LSR-3. The electrical conductivity ($\sigma$) is measured in a Linseis LSR-3 using a four-probe configuration and re-confirmed using a Van der-Pauw method in a MMR system. The thermal conductivity ($\kappa$) is expressed as $\kappa = D_T \cdot C_p \cdot \rho$. Thermal diffusivity ($D_T$) is measured using laser flash method in a Linseis XFA 600. Specific Heat ($C_p$) is measured on a Linseis DSC using sapphire as the standard. Mass density ($\rho$) is calculated from the sample mass and dimensions. The deviation of $S$ is around 2%, electrical conductivity $\sigma$ (5%) and thermal conductivity $\kappa$ (5%). The combined uncertainty of $zT$ ($S^2\sigma T/\kappa$) is around 15%.

**Characterizations of intermediate products during the synthesis of PbTe-$Bi_2Te_3$ nanoheterostructure**

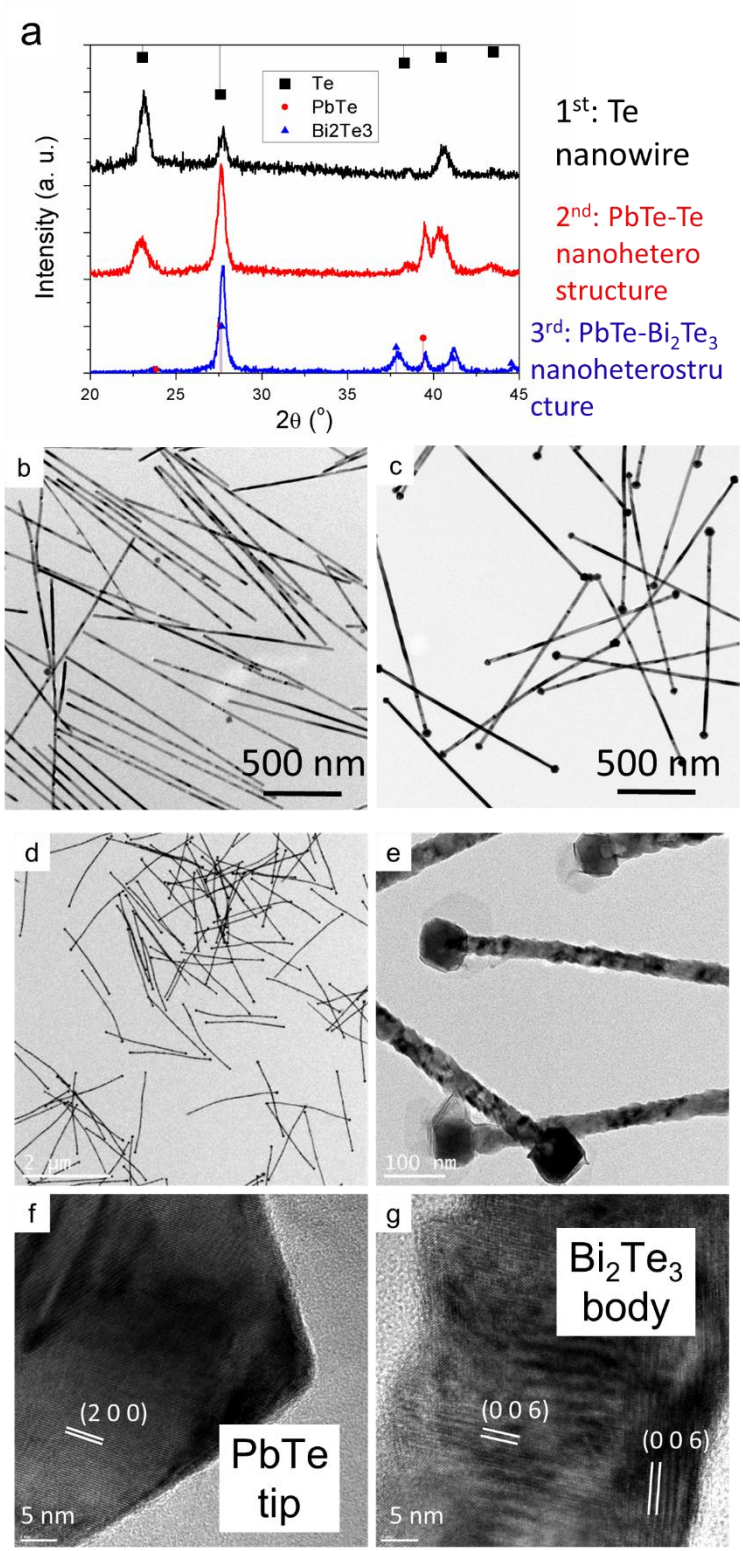


Figure S1. (a) XRD profiles of Te nanowire in the 1st step, 0.10 PbTe-0.90 Te nanoheterostrucutre in the 2nd step and 0.10 PbTe-0.90$Bi_2Te_3$ nanoheterostructure in the 3rd step of synthesis. TEM images of (b) Te nanowire, (c) 0.10 PbTe-0.90 Te nanoheterostrucutre and (d), (e) 0.10 PbTe-0.90$Bi_2Te_3$ nanoheterostructure. (f), (g): HRTEM of 0.10 PbTe-0.90 $Bi_2Te_3$ nanoheterostructure showing the tip of PbTe and body of $Bi_2Te_3$.

**Characterizations of as-sintered nano $PbBi_{2n}Te_{1+3n}$ samples**

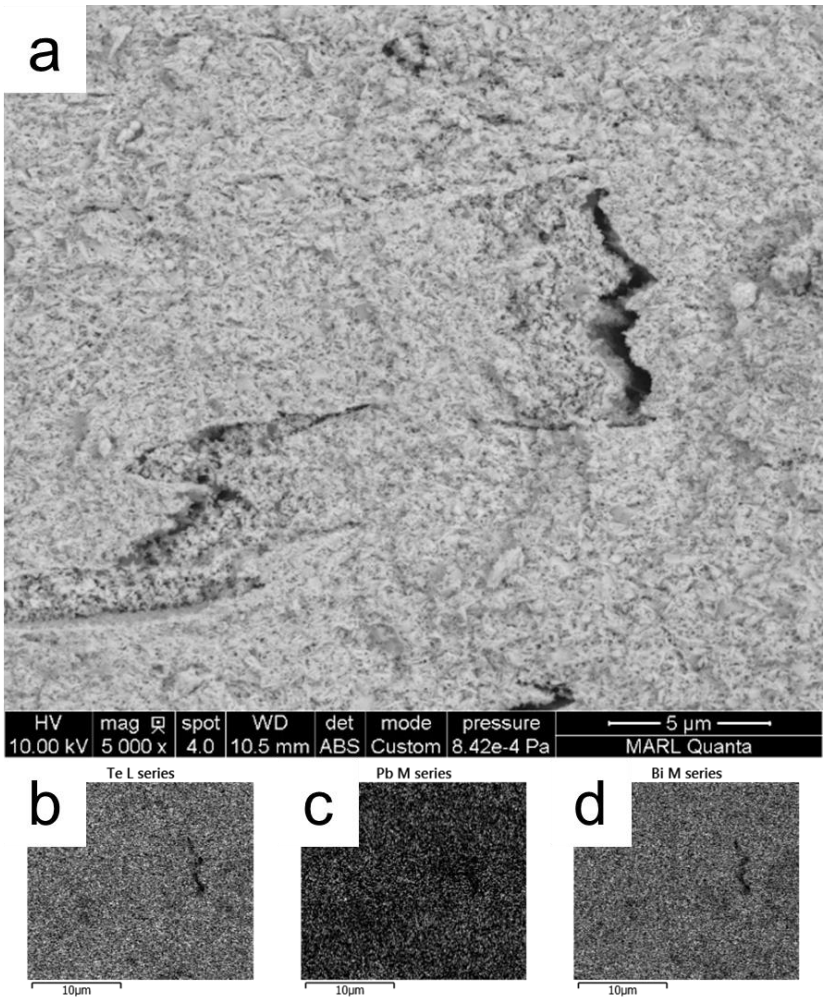


Figure S2. (a) SEM (back-scattered mode) image of the fractured nano $PbBi_4Te_7$ sample. EDS mappings of (b) Te, (c) Pb and (d) Bi elements.

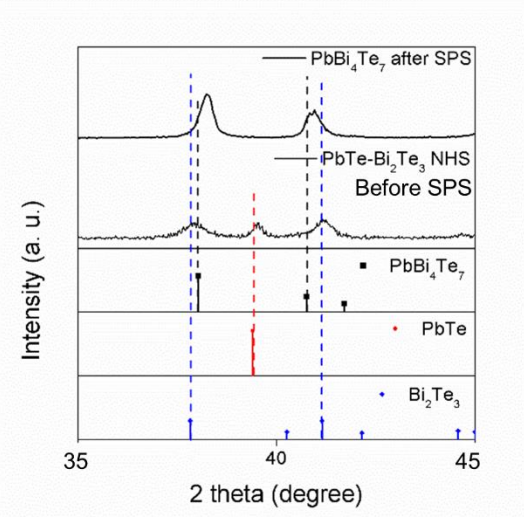


Figure S3. Magnified view of XRD profiles of 0.14286 PbTe-0.85714 $Bi_{0.666}Te$ nanoheterostructure before SPS and nano $PbBi_4Te_7$ after SPS samples.

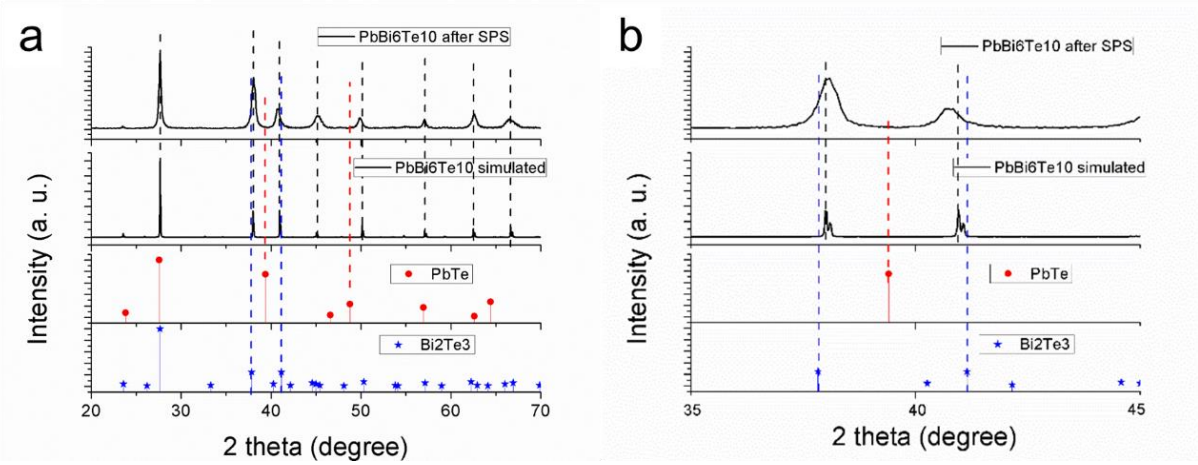


Figure S4. (a) XRD profile of the nano $PbBi_6Te_{10}$ sample and (b) the magnified view from 35-45 degree. The peaks of nano $PbBi_6Te_{10}$ sample shifted a little bit with respect to the standard lines of simulated bulk-phase $PbBi_6Te_{10}$ (atomic structure shown in Figure 1e of main text) because of the deviation of nano-phase atomic structure as compared to bulk-phase.

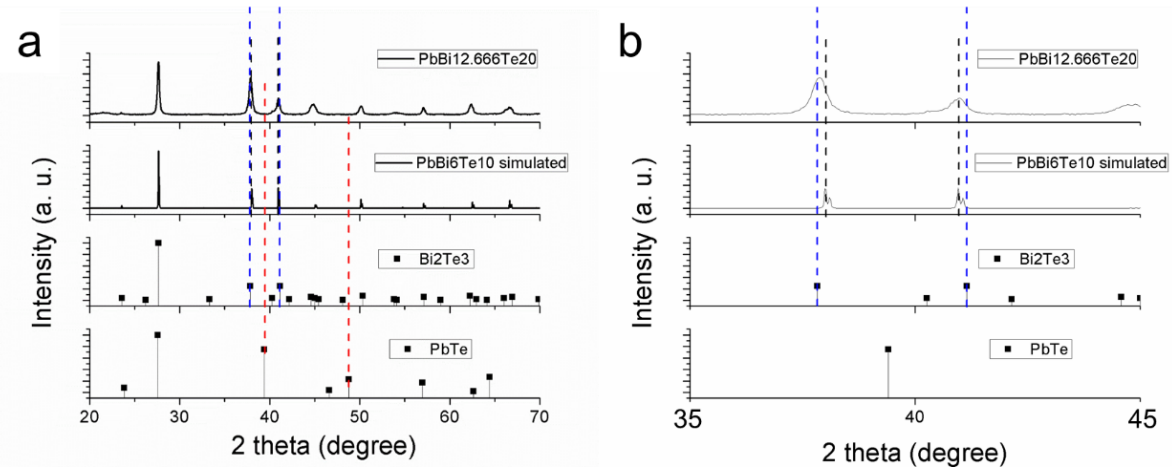


Figure S5. (a) XRD profile of the nano $PbBi_{12.6666}Te_{20}$ sample and (b) the magnified view from 35-45 degree. Since there is no reported atomic structure and standard XRD lines of $PbBi_{12.6666}Te_{20}$, we compare the XRD profile of the nano $PbBi_{12.6666}Te_{20}$ with those of $PbBi_6Te_{10}$ and $Bi_2Te_3$. The peaks of the nano $PbBi_{12.6666}Te_{20}$ sample are located between the peaks of $PbBi_6Te_{10}$ (black dashed lines) and $Bi_2Te_3$ (blue dashed lines).

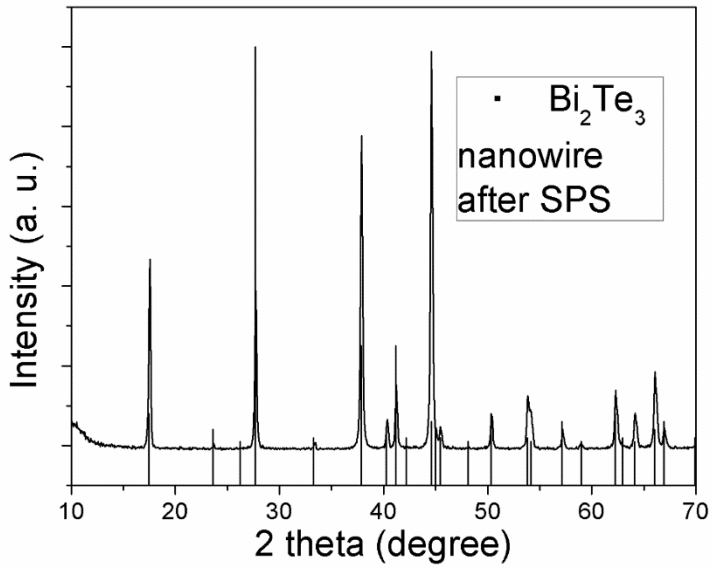


Figure S6. XRD profile of the 'nano $Bi_2Te_3$ after SPS' sample. All the peaks agree with the standard lines of JCPDS NO. 15-0863 (Rhombohedral $Bi_2Te_3$).

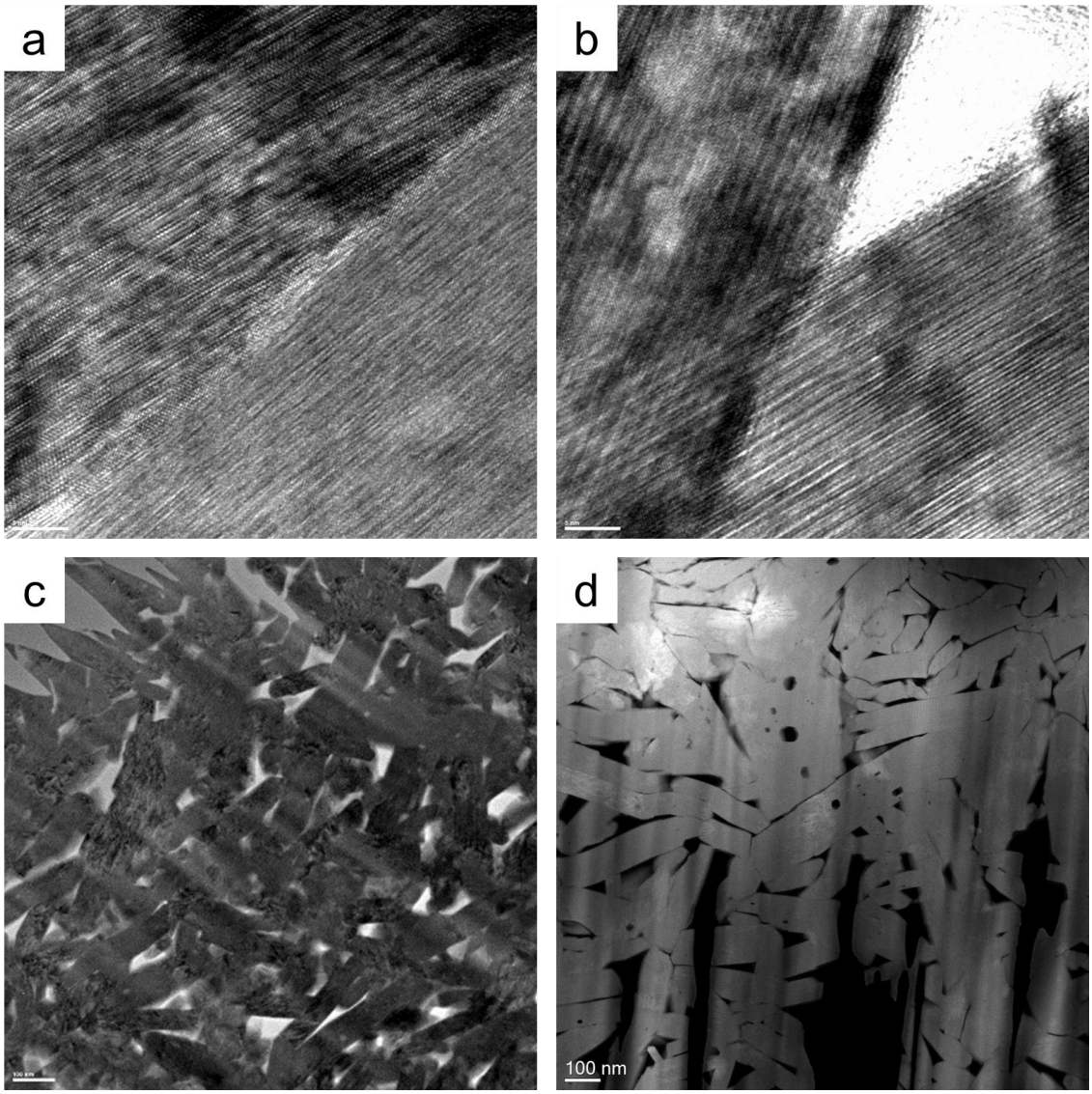


Figure S7. HRTEM images of a) nano $PbBi_6Te_{10}$ and b) nano $PbBi_4Te_7$ samples, clearly showing the layered crystal structures, both the scale bars are 5 nm. C) TEM image of nano $PbBi_6Te_{10}$ sample and d) HAADF-STEM image of nano $PbBi_4Te_7$ samples, the scale bars in c) and d) are both 100 nm.

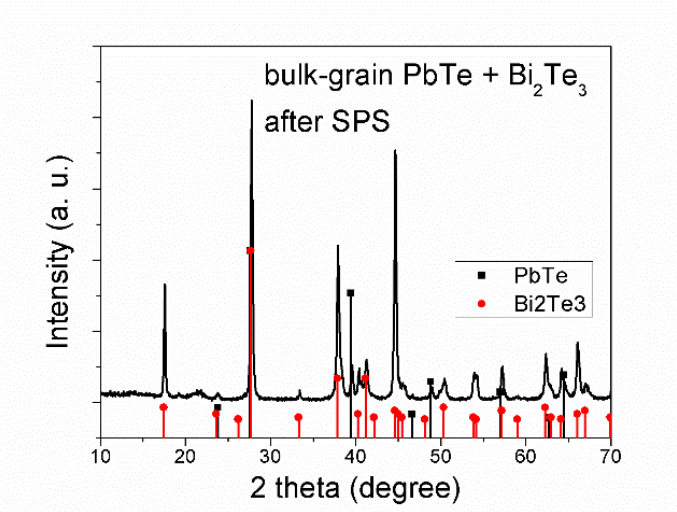


Figure S8. XRD profile of the 'Bulk PbTe + $Bi_2Te_3$ after SPS' sample showing only the peaks of PbTe and $Bi_2Te_3$, without any discernible peaks of $PbBi_4Te_7$, indicating that no solid-state reaction happened.

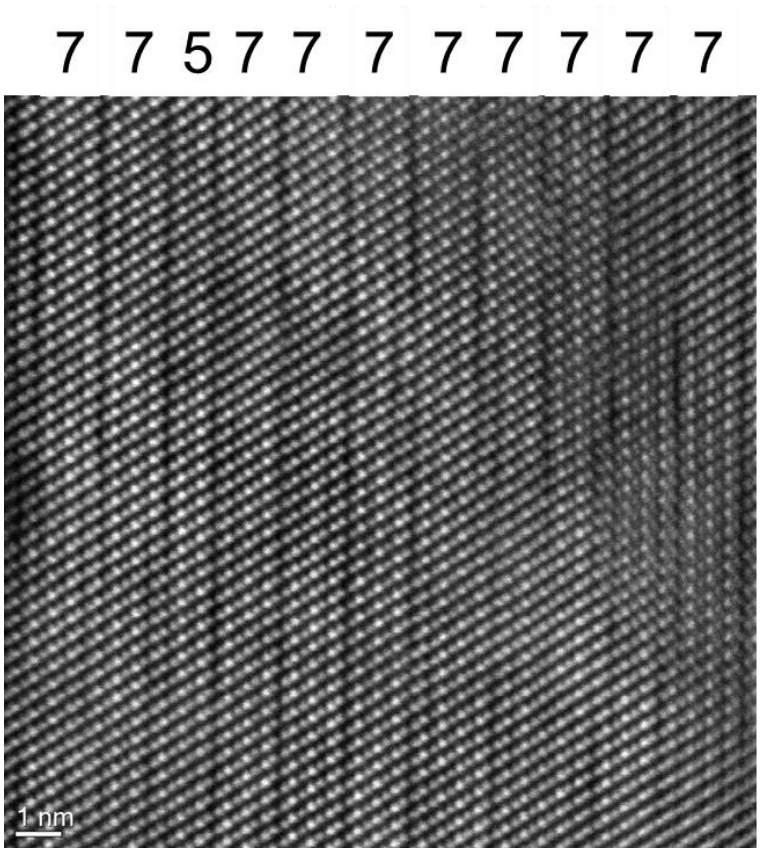


Figure S9. HADDF-STEM images of nano $PbBi_4Te_7$ sample showing the 5-7 randomness. Scale bar is 1 nm.

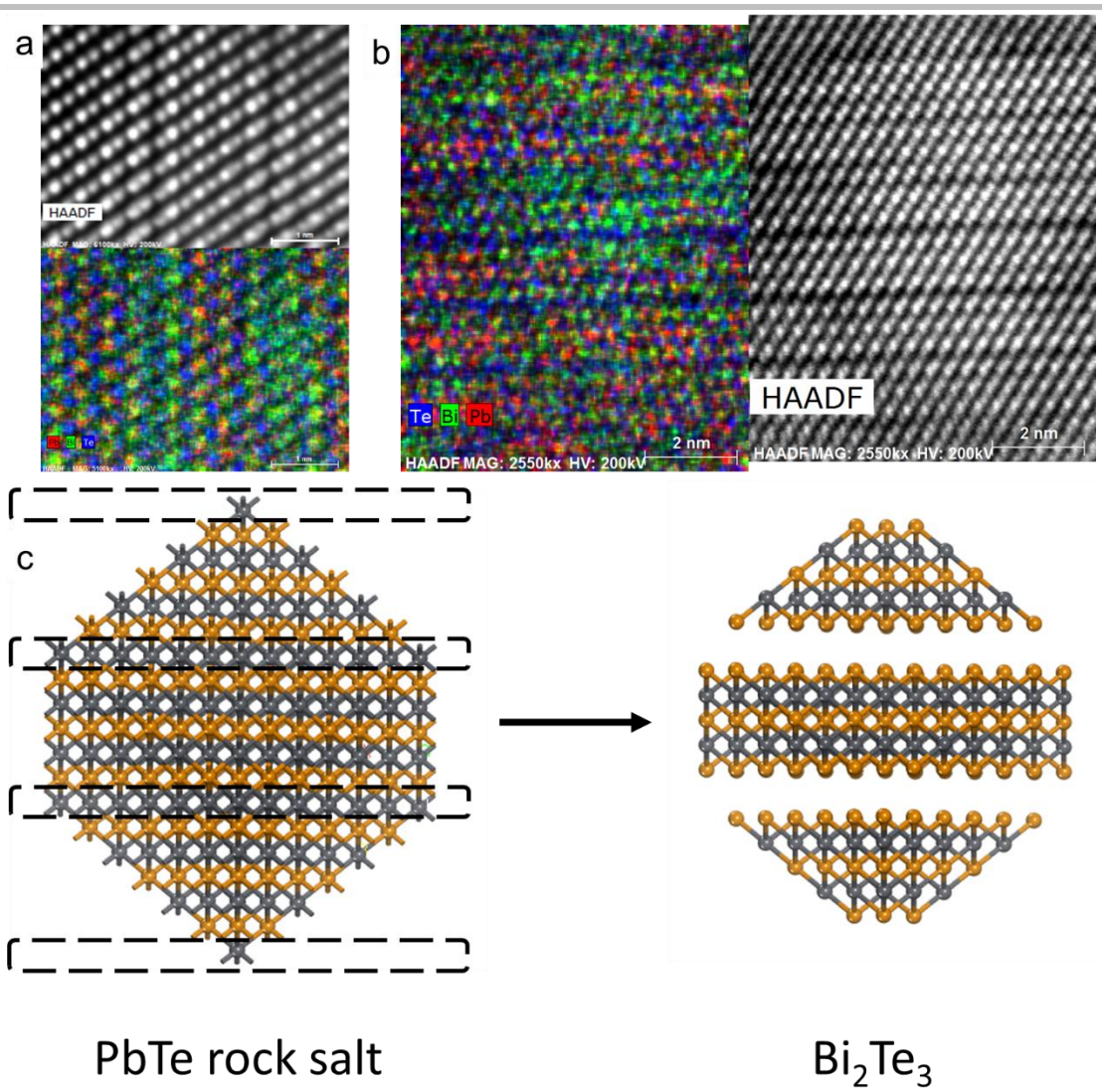


Figure S10. Atomic-level EDS mapping of (a) $PbBi_6Te_{10}$ and (b) $PbBi_4Te_7$ over a large area, The Red, Green and Blue dots correspond to Pb, Bi and Te atoms, respectively. (c) Illustration of the relationship between PbTe and $Bi_2Te_3$ in terms of crystal structure.

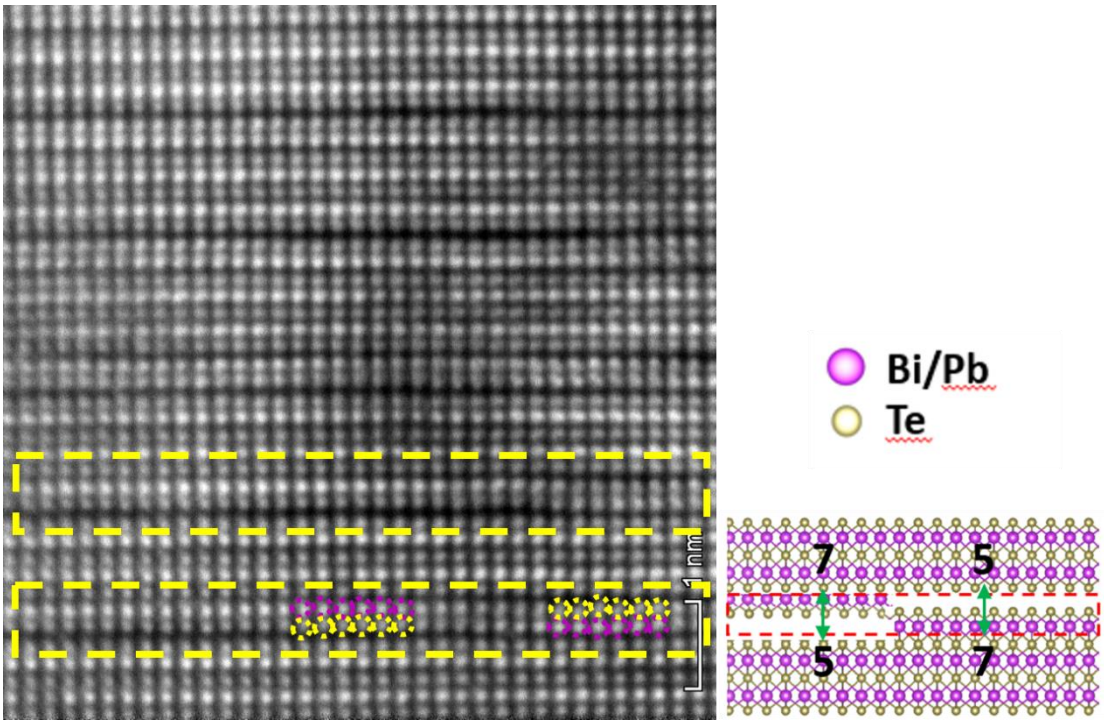


Figure S11. Left: The HAADF-STEM images of nano $PbBi_4Te_7$ sample. Zipper-like structures are highlighted in the yellow dashed box. Purple and yellow dashed circles in (b) represent Bi (brighter) and Te (darker) atoms, respectively, whose sites gradually exchange with each other at the boundary of zipper-like structures. Right: The scheme showing the mechanism of the formation of zipper-like van der waals gap discontinuity between quintuple and septuple layers in $PbBi_4Te_7$.

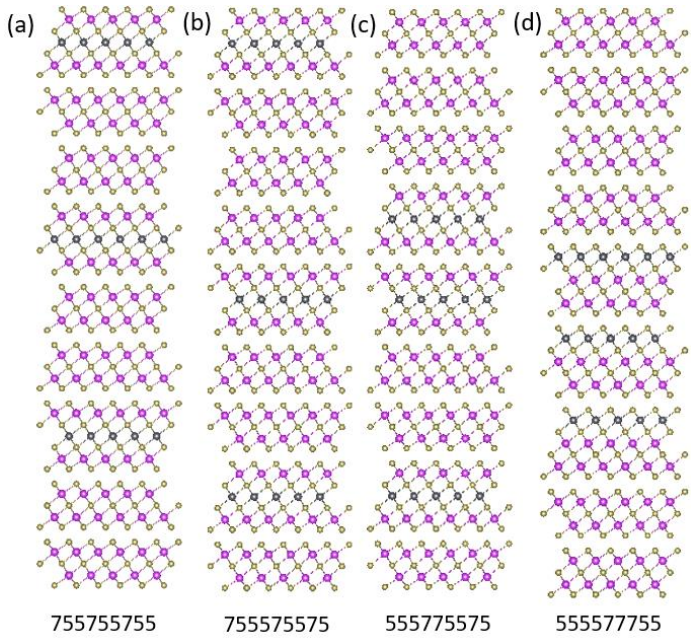


Figure S12. (a) $PbBi_6Te_{10}$ single crystal structure. (b, c, d) crystal structures of $PbBi_6Te_{10}$ with random thickness arrangement of the quintuple (5) and septuple (7) layers. The Pb, Bi and Te atoms are represented by the grey, purple and yellow balls, respectively.

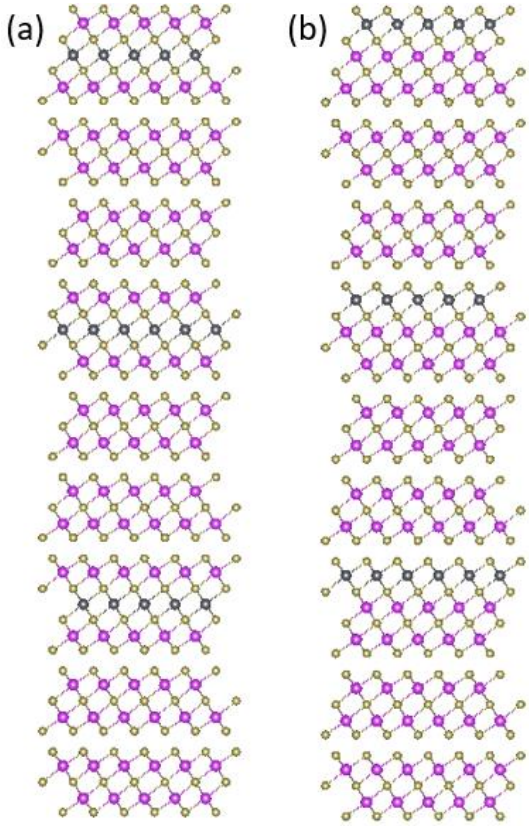


Figure S13. (a) $PbBi_6Te_{10}$ single crystal structure. (b) the structure after exchanging one Pb layer (black) with a Bi layer, illustrating the Pb/Bi site randomness. The Pb, Bi and Te atoms are represented by the grey, purple and yellow dots, respectively.

To explain the observation that Pb atoms are distributed dispersively in the Pb/Bi sites rather than staying in particular atomic rows, we have conducted DFT simulations in which a whole Pb layer is exchanged with a whole Bi layer (Figure S13). It is found that the energy difference is 0.040 eV/atom and smaller than the thermal fluctuation (698 K, $k_BT$ = 0.060 eV). This indicates that the preference of Pb location is not strong during the SPS.

**Anisotropy in thermoelectric properties of the nano $PbBi_4Te_7$ sample**

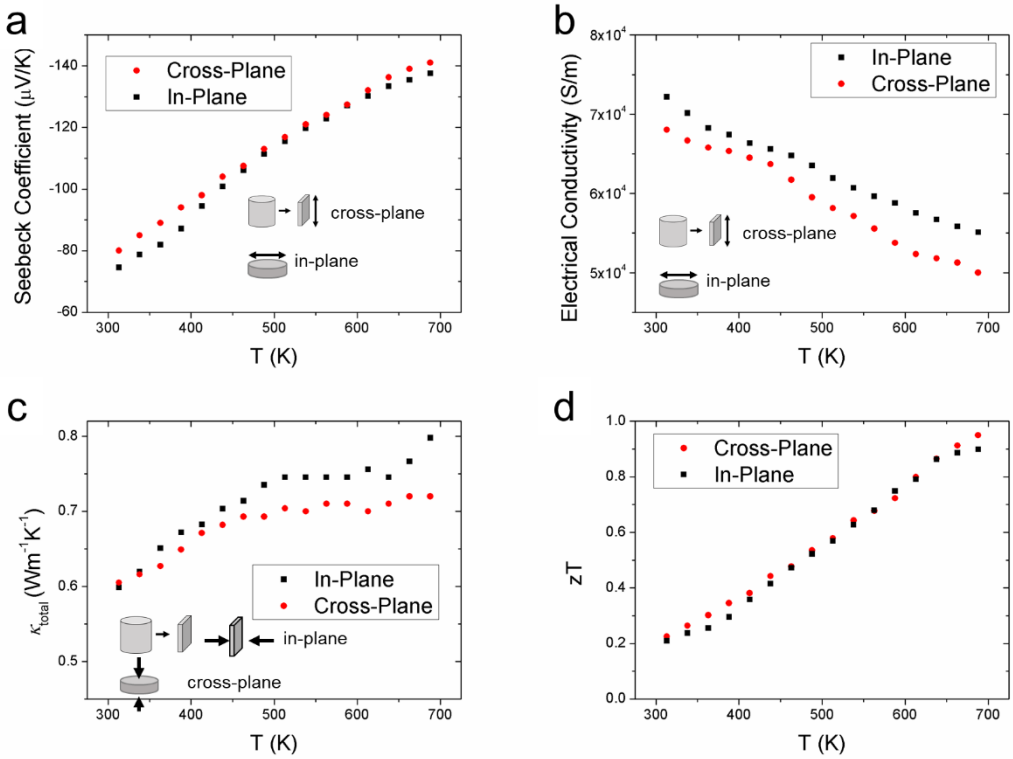


Figure S14. Temperature-dependent (a) Seebeck coefficient, (b) electrical conductivity, (c) thermal conductivity and (d) figure of merit of the nano $PbBi_4Te_7$ sample along the in-plane (black squares) and cross-plane directions (red circles).

# Phonon Boltzmann Transport Equation Modeling

The lattice thermal conductivity is calculated by the Boltzmann transport equation[1,2],

$$\kappa_{lat} = \frac{1}{N_{\mathbf{q}} V_{cell}} (1-P)^{3/2} \frac{1}{3} \sum_{j}^{15} \sum_{\mathbf{q}}^{4096} \sum_{\alpha}^{x,y,z} \frac{\hbar^2 \omega^2(\mathbf{q}, j)}{k_B T^2} \frac{e^{\frac{\hbar\omega(\mathbf{q}, j)}{k_B T}}}{(e^{\frac{\hbar\omega(\mathbf{q}, j)}{k_B T}} - 1)^2} \upsilon_{ph,\alpha}{}^2(\mathbf{q}, j) \tau_{ph}(\mathbf{q}, j) \quad \text{(S1)}$$

$$\frac{1}{\tau_{ph}(\mathbf{q}, j)} = \frac{1}{\tau_{ah}(\mathbf{q}, j)} + \frac{1}{\tau_{Pb-Bi}(\mathbf{q}, j)} + \frac{1}{\tau_{gb}(\mathbf{q}, j)}. \quad \text{(S2)}$$

where $\hbar$ is the Plank constant, $k_B$ is the Boltzmann constant, $T$ is temperature in Kelvin, $\omega$ is the phonon angular frequency, $\mathbf{q}$ is the phonon wavevector, $j$ is the phonon branch, $\alpha$ stands for $x$, $y$ and $z$ directions, $v_{ph,\alpha}$ is the phonon group velocity component in the direction $\alpha$. $N_{\mathbf{q}}$ is the number of $\mathbf{q}$ points sampled uniformly throughout the first Brillouin Zone (16×16×16 = 4096 in our simulations), and $V_{cell}$ is the volume of a primitive cell. The summation is taken over all the phonon modes ($\mathbf{q}$, $j$). $P$ is the porosity, and the factor $(1-P)^{3/2}$ takes into account of the loss of material by effective medium theory[3]. $\tau_{ph}$ is the phonon relaxation time, which involves multiple phonon scattering processes including anharmonic phonon scattering ($\tau_{ph}^{-1}$), phonon-Pb/Bi mass disorder scattering ($\tau_{Pb-Bi}^{-1}$), and phonon grain-boundary scattering ($\tau_{gb}^{-1}$). In Eq. (S1), the summation over $j$ is taken over all the phonon branches. Since there is no full dispersion relaxation available for the large unit-cell material $PbBi_{2n}Te_{1+3n}$ (n =2 or 3), we use the phonon dispersion of $Bi_2Te_3$ instead, and treat Pb as the mass-disorder induced in $Bi_2Te_3$. Although using the dispersion of $PbBi_{2n}Te_{1+3n}$ (n =2 or 3) might be more accurate, the choice of phonon dispersion is not critical since the model parameters will be calibrated by the measured thermal conductivity of bulk single-crystal $PbBi_{2n}Te_{1+3n}$ in literature[13] (E. Shelimova, et al, *Inorganic Materials* **2004**, 40, 451-460). The effect of mass-disorder, nano grain boundaries and pores will be calculated based on the calibrated model parameters. An alternative and easier way is to replace the full dispersion with a single Debye mode by using Debye-Callaway model, which has been widely used[4,5]. However, here, we still prefer to use the full dispersion of $Bi_2Te_3$ rather than the Debye model since the latter one only considers the acoustic branches and will significantly underestimate the thermal conductivity[6].

To obtain the lattice thermal conductivity by Eq. (S1), we have conducted first-principle calculations using density functional theory (DFT) to calculate the phonon dispersion relations. DFT was implemented via the VASP program package[7,8], employing the projector augmented wave method (PAW) under local density approximation. The structures were relaxed via the primitive unit cell with a convergence of $10^{-7}$ eV for the total energy, and $10^{-5}$ eV/Å for the forces on each atom. The relaxed

lattice constants for $Bi_2Te_3$ are a=4.3550 Å, c= 29.8887 Å, which agree well with the literature[9,10]. The plane-wave energy cutoff is 500 eV. The electronic k-space integration was performed with the tetrahedron method, involving a $\Gamma$-centered 12×12×12 k-mesh. The phonon dispersion is calculated via 2×2×2 primitive cells (40 atoms) by the density functional perturbation theory (DFPT) using the PHONOPY package[11] with a Γ-centered 6 × 6 × 6 k-mesh. Spin-orbital coupling is not included as it is not critical for lattice vibration properties[6,9,10]. The calculated phonon dispersion relations are show in Fig. S15, which agrees well with literature[6,9,10].

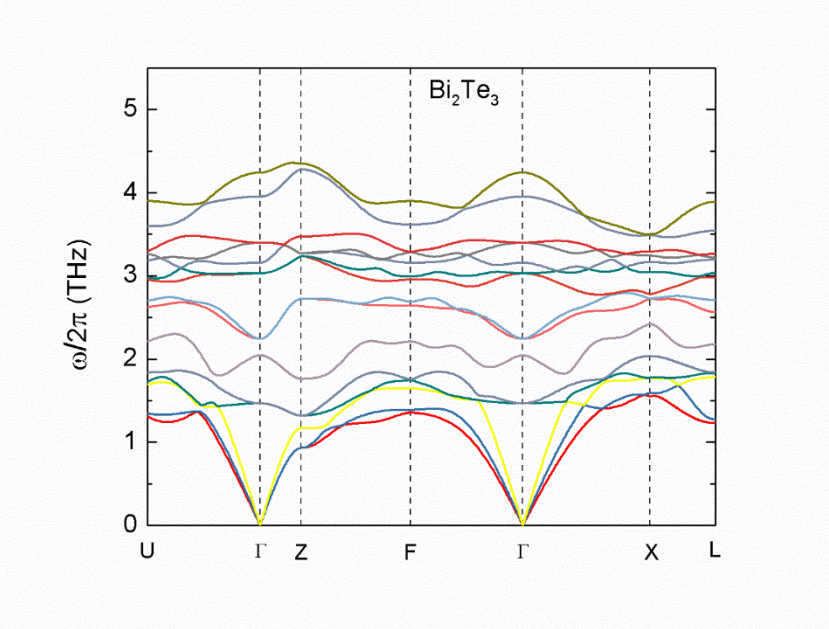


Figure S15. Phonon band dispersion of $Bi_2Te_3$ calculated from DFT.

The anharmonic phonon scattering rate is calculated by

$$\frac{1}{\tau_p(\mathbf{k},j)} = \frac{Ak_BT}{M_a v^2(\mathbf{k},j)} \frac{\gamma^2\omega^2(\mathbf{k},j)}{\omega_{\max}(j)} \exp\left(-\frac{\hbar\omega_{\max}(j)}{3k_BT}\right). \quad \text{(S3)}$$

For the phonon-phonon scattering[1] in Eq. (S3), $\omega(\mathbf{k},j)$ and $v(\mathbf{k},j)$ are the spectral phonon frequency and velocity, respectively. $\omega_{max}(j)$ is the maximum frequency of the phonon branch $j$. $\gamma$ is the Grüneisen parameter with the value of 1.5 [12]. $M_a$ is the average atomic mass given by

$$M_a = \frac{\alpha_{Pb}M_{Pb} + \alpha_{Bi}M_{Bi} + \alpha_{Te}M_{Te}}{\alpha_{Pb} + \alpha_{Bi} + \alpha_{Te}}, \quad \text{(S4)}$$

where $\alpha$ is the stoichiometric coefficient. The values of coefficient $A$ for $PbBi_4Te_7$ and $PbBi_6Te_{10}$ are determined by the experimental room-temperature lattice thermal conductivities values, 0.70 W/mK and 0.85 W/mK, respectively[13].

The Pb-Bi mass disorder scattering is calculated by

$$\frac{1}{\tau_{Pb}(\mathbf{k},\nu)} = \frac{\pi}{2} n_{Pb}(1-\frac{M_{Pb}}{M_{Bi}})^2 \omega^2(\mathbf{k},\nu) DOS(\omega). \quad \text{(S5)}$$

$DOS(\omega)$ is the normalized phonon density of states. $n_{Pb}$ is the Pb concentration.

The grain boundary scattering is give by[1]

$$\frac{1}{\tau_b(\mathbf{k},\nu)} = \frac{v(\mathbf{k},\nu)}{D}. \quad \text{(S6)}$$

$D$ is the grain diameter given by $D = \left(\frac{6}{\pi} L_x L_y L_z\right)^{1/3}$, where $L_x$, $L_y$ and $L_z$ are the dimensions of nanograins.

The parameters are listed in Table S1.

Table S1. Parameters used in the modeling of lattice thermal conductivity

| Parameters | $PbBi_4Te_7$ | $PbBi_6Te_{10}$ |
|---|---|---|
| $P$ (porosity) | 16% | 16% |
| Fitting parameter A | 6.44 | 5.306 |
| Grain size $L_x$, $L_y$ (nm) | 250 | 100 |
| Grain size $L_z$ (nm) | 140 | 70 |
| Grain diameter (nm) | 229 | 139 |

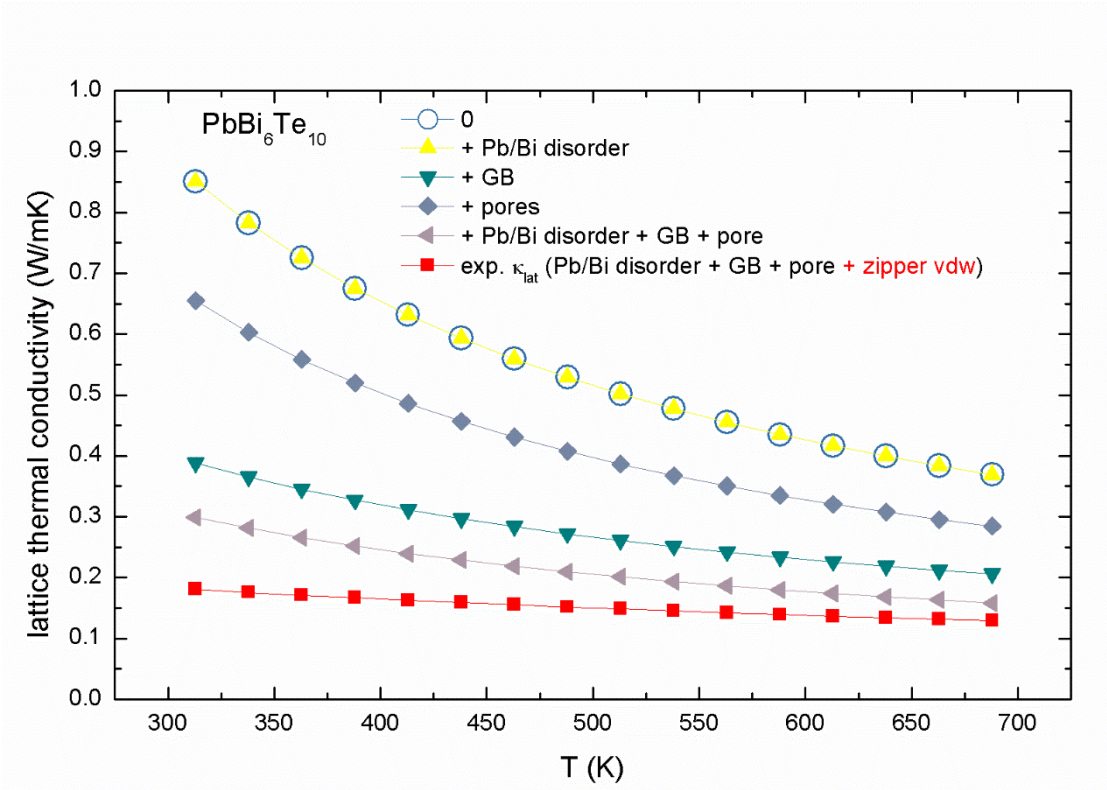


Figure S16. Lattice thermal conductivity modeled by phonon BTE for nano $PbBi_6Te_{10}$ sample. The red curve stands for experimental ($k_{tot}$-$k_e$).

**Molecular Dynamics Simulations**

Molecular dynamics simulations of $Bi_2Te_3$ was conducted using LAMMPS package[14]. The potential was developed by Qiu and Ruan[15]. To study the impact of layer-thickness randomness on the thermal transport, we changed part of the mass of $Bi_2Te_3$ layers to the mass of 'Bi+Te+Pb+Te' to simulate the insertion of PbTe layer. The thermal conductivity is calculated by Green-Kubo method[16]. For the two models shown in Fig. S17, the calculated thermal conductivity along the c axis is 0.42 and 0.30 W/mK, respectively. The thermal conductivity of the $PbBi_4Te_7$ superlattice (0.42 W/mK) is smaller than that of pure $Bi_2Te_3$ along the c axis (about 0.70 W/mK) as calculated in Ref.[15] due to the introduction of mass disorder. The RML thermal conductivity (0.30 W/mK) is even smaller than the superlattice (0.42 W/mK) due to the break of coherence, similar to the results observed in imaginary Lennard-Jones superlattice[14] and Si/Ge superlattices[15].

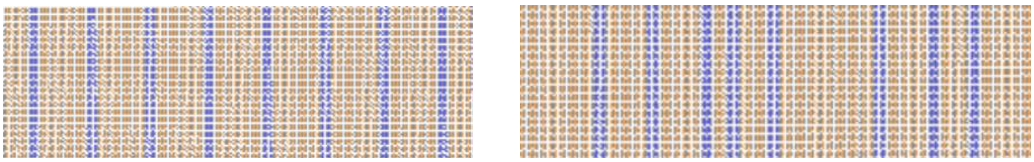

Figure S17. The simulated structures: (left) Superlattice, (right) random multilayer. The blue columns represent the $Bi_2Te_3$ layers with changed mass due to alloying with Pb.

## References


1. Feng, T. & Ruan, X. Prediction of Spectral Phonon Mean Free Path and Thermal Conductivity with Applications to Thermoelectrics and Thermal Management: A Review. *J. Nanomater.* **2014,** 206370 (2014).
2. Dettori, R., Melis, C., Cartoixà, X., Rurali, R. & Colombo, L. Model for thermal conductivity in nanoporous silicon from atomistic simulations. *Phys. Rev. B* **91,** 054305 (2015).
3. Bauer, T. A general analytical approach toward the thermal conductivity of porous media. *Int. J. Heat Mass Transf.* **36,** 4181–4191 (1993).
4. Hong, M. *et al.* n-Type Bi2Te3-xSex Nanoplates with Enhanced Thermoelectric Efficiency Driven by Wide-Frequency Phonon Scatterings and Synergistic Carrier Scatterings. *ACS Nano* **10,** 4719–4727 (2016).
5. Kim, S. I. *et al.* Dense dislocation arrays embedded in grain boundaries for high-performance bulk thermoelectrics. *Science* **348,** 109–114 (2015).
6. Hellman, O. & Broido, D. a. Phonon thermal transport in Bi2Te3 from first principle. *Phys. Rev. B* **90,** 134309 (2014).
7. Kresse, G. & Hafner, J. Ab initio molecular dynamics for liquid metals. *Phys. Rev. B* **47,** 558 (1993).
8. Kresse, G. & Furthmüller, J. Efficient iterative schemes for ab initio total-energy calculations using a plane-wave basis set. *Phys. Rev. B* **54,** 11169–11186 (1996).
9. Chis, V. *et al.* Vibrations in binary and ternary topological insulators: First-principles calculations and Raman spectroscopy measurements. *Phys. Rev. B* **86,** 174304 (2012).
10. Chen, X., Parker, D. & Singh, D. J. Acoustic impedance and interface phonon scattering in Bi2Te 3 and other semiconducting materials. *Phys. Rev. B - Condens. Matter Mater. Phys.* **87,** 045317 (2013).
11. Togo, A., Oba, F. & Tanaka, I. First-principles calculations of the ferroelastic transition between rutile-type and CaCl2-type SiO2 at high pressures. *Phys. Rev. B* **78,** 134106 (2008).
12. Bessas, D. *et al.* Lattice dynamics in Bi2Te3 and Sb2Te 3: Te and Sb density of phonon states. *Phys. Rev. B - Condens. Matter Mater. Phys.* **86,** 224301 (2012).
13. Shelimova, L. E. *et al.* Crystal structures and thermoelectric properties of layered compounds in the ATe--Bi 2 Te 3 (A= Ge, Sn, Pb) systems. *Inorg. Mater.* **40,** 451–460 (2004).
14. Plimpton, S. Fast parallel algorithms for short-range molecular dynamics. *J. Comput. Phys.* **117,** 1–19 (1995).
15. Qiu, B. & Ruan, X. L. C.-165203. Molecular dynamics simulations of lattice thermal conductivity of bismuth telluride using two-body interatomic potentials. *Phys. Rev. B* **80,** 165203 (2009).
16. McGaughey, A. J. H. & Kaviany, M. Phonon transport in molecular dynamics simulations: Formulation and thermal conductivity prediction. *Adv. Heat Transf.* **39,** 169–255 (2006).


## Author Contributions

Biao Xu and Zhe Li performed the synthesis of nanocrystal, XRD, SEM and thermoelectric measurements. Lin Zhou conducted TEM. Tianli Feng and Sokrates T. Pantelides performed the DFT, MD and BTE calculations. Biao Xu, Sokrates T. Pantelides and Yue Wu supervised the work.